

# Chaperone-derived copper(I)-binding peptide nanofibers disrupt copper homeostasis in cancer cells

Jeena M.T.<sup>1</sup>, Julian Link<sup>1</sup>, Jian Zhang<sup>1</sup>, Iain Harley<sup>1</sup>, Petri Turunen<sup>3</sup>, Robert Graf<sup>1</sup>, Manfred Wagner<sup>1</sup>, Luis Andre Baptista<sup>1</sup>, Hendrik R. A. Jonker<sup>4</sup>, Liyang Cui<sup>2</sup>, Ingo Lieberwirth<sup>1</sup>, Katharina Landfester<sup>1</sup>, Jianghong Rao<sup>2\*</sup>, David Y. W. Ng<sup>1\*</sup>, Tanja Weil<sup>1\*</sup>

<sup>1</sup>Max-Planck Institute for Polymer Research, Ackermannweg 10, 55128 Mainz, Germany.

<sup>2</sup>Department of Radiology, Molecular Imaging Program at Stanford, Stanford University School of Medicine, Stanford, CA 94305, USA.

<sup>3</sup>Microscopy Core Facility, Institute of Molecular Biology (IMB), Ackermannweg 10, 55128 Mainz, Germany.

<sup>4</sup>Institute for Organic Chemistry and Chemical Biology, Center for Biomolecular Magnetic Resonance (BMRZ), Goethe University Frankfurt, 60438 Frankfurt am Main, Germany.

**Abstract:** Copper (Cu) is a transition metal that plays crucial roles in cellular metabolism. Cu<sup>+</sup> homeostasis is upregulated in many cancers and contributes to tumorigenesis. However, therapeutic strategies to target Cu<sup>+</sup> homeostasis in cancer cells are rarely explored because small molecule Cu<sup>+</sup> chelators have poor binding affinity in comparison to the intracellular Cu<sup>+</sup> chaperones, enzymes, or ligands. To address this challenge, we introduce a Cu<sup>+</sup> chaperone-inspired supramolecular approach to disrupt Cu<sup>+</sup> homeostasis in cancer cells that induces programmed cell death. The **Nap-FFMTCGGCR** peptide self-assembles into nanofibers inside cancer cells with high binding affinity and selectivity for Cu<sup>+</sup> due to the presence of the unique **MT/CGGC** motif, which is conserved in intracellular Cu<sup>+</sup> chaperones. **Nap-FFMTCGGCR** exhibits cytotoxicity towards triple negative breast cancer cells (MDA-MB-231), impairs the activity of Cu<sup>+</sup> dependent co-chaperone super oxide dismutase1 (SOD1), and induces oxidative stress. In contrast, **Nap-FFMTCGGCR** has minimal impact on normal HEK 293T cells. Control peptides show that the self-assembly and Cu<sup>+</sup> binding must work in synergy to successfully disrupt Cu<sup>+</sup> homeostasis. We show that assembly-enhanced affinity for metal ions opens new therapeutic strategies to address disease-relevant metal ion homeostasis.

## Introduction

Metal ions are indispensable for multiple cellular functions including signal transduction, chemical reactions, and structural components of biomacromolecules.<sup>1</sup> Copper (Cu) is a redox-active transition metal serving as an enzyme co-factor mediating metabolic processes essential for cellular growth and development including antioxidant defense<sup>2</sup>, aerobic respiration<sup>3</sup>, iron transport<sup>4</sup>, and other processes such as pigment synthesis.<sup>5</sup> The availability of intracellular, unbound Cu ions is controlled tightly to avoid oxidative stress, lipid peroxidation and non-specific binding to intracellular biomolecules.<sup>6-7</sup> Hence, the cytoplasmic concentration of free Cu ions is exceedingly low, between 10<sup>-15</sup> to 10<sup>-21</sup> M.<sup>8</sup> To maintain cellular Cu homeostasis, cells have evolved sophisticated trafficking pathways consisting of transporters, ligands, chaperones, and their respective counter proteins (co-chaperones).<sup>9-10</sup>

Extracellular  $\text{Cu}^{2+}$  is reduced to  $\text{Cu}^+$  by the six transmembrane epithelial antigen of prostate (STEAP) family metalloredutase proteins located in the plasma membrane.<sup>11</sup> Then, cellular uptake is mediated by the high affinity  $\text{Cu}^+$  transmembrane transporter protein Ctr1 (SLC31A1).<sup>12</sup> The predominant oxidation state of Cu in the cell is +1 due to the reductive cellular environment.<sup>13</sup> Once  $\text{Cu}^+$  is transported into the cell, cytosolic GSH binds free  $\text{Cu}^+$  and forms  $\text{Cu}^{\text{I}}$ -GSH complex to minimize the availability of free  $\text{Cu}^+$  ions and to create an exchangeable pool of  $\text{Cu}^+$ .<sup>8</sup> The  $\text{Cu}^{\text{I}}$ -GSH complex transfers  $\text{Cu}^+$  to the cytosolic  $\text{Cu}^+$  chaperones, such as antioxidant 1 (Atox1), cyclooxygenase17 (COX17) and copper chaperone for superoxide dismutase (CCS).<sup>14-15</sup> The  $\text{Cu}^+$  trafficking pathways in human cells consist of high chaperone-protein specificity following an affinity gradient.<sup>16</sup> Briefly,  $\text{Cu}^+$  transfer takes place from Atox1 to ATPase  $\text{Cu}^+$  transporting alpha/beta (ATP7A/7B) located at the trans-Golgi network, from COX17 to mitochondrial synthesis of cytochrome oxidase 1/2 (Sco1/2) or cytochrome C oxidase (CCO), and from CCS to SOD1 located in the cytosol or in the mitochondrial inner membrane (Figure 1A).<sup>17</sup> The chaperones bind to  $\text{Cu}^+$  via the cysteine residues of a conserved **MT/CXXC** (X is an arbitrary amino acid) domain present in intracellular  $\text{Cu}^+$  chaperones and  $\text{Cu}^+$  exchange proceeds through a thiol exchange mechanism (Figure 1A).<sup>18</sup>

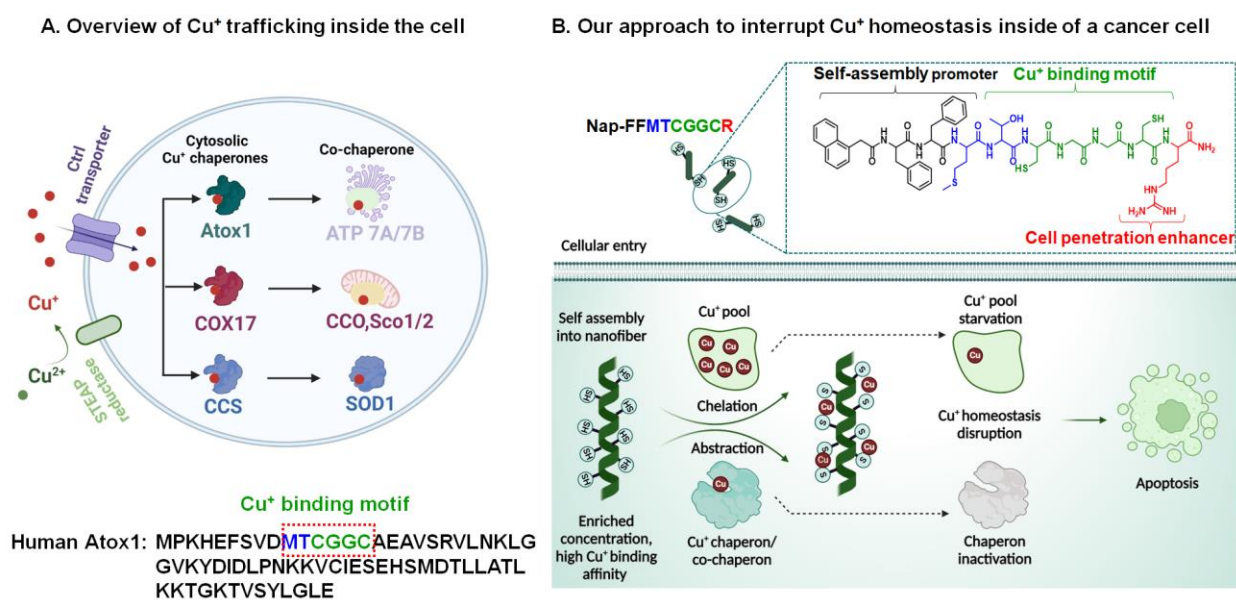


**Figure 1:** A) Schematic illustration of  $\text{Cu}^+$  uptake and trafficking in human cells. Complete sequence of Atox1 possessing **MT/CGGC** as  $\text{Cu}^+$ -binding domain is shown. B)  $\text{Cu}^+$  chaperone-derived peptide **Nap-FFMTCGGCR** self-assembles into nanofibers inside the cancer cells, with multiple copies of  $\text{Cu}^+$ -binding motif arranged along the surface of the fiber. These fibers then bind to  $\text{Cu}^+$  and disrupt the intracellular  $\text{Cu}^+$  trafficking of cancer cells. **Nap-FFMTCGGCR** fibers capture  $\text{Cu}^+$  ions from the intracellular pool or  $\text{Cu}^+$  chaperones, resulting in an overall deprivation of  $\text{Cu}^+$  bioavailability. This deprivation induces oxidative stress, cellular dysfunction, and ultimately apoptosis.

Imbalances in  $\text{Cu}^+$  homeostasis induces abnormalities, which are indicated in the pathogenesis of several diseases including cancer,<sup>19</sup> Wilson disease (WD),<sup>20</sup> and Menkes disease.<sup>21</sup> For example,

Cu<sup>+</sup> is involved in cancer cell proliferation, immune system modulation and angiogenesis of the tumor growth and development,<sup>22</sup> including colorectal,<sup>23</sup> lung,<sup>24</sup> breast,<sup>25</sup> primary brain,<sup>26</sup> hepatocellular carcinoma<sup>27</sup> etc. Recently, a new concept of “cuproplasia” has been introduced, defined as Cu-dependent cell growth and proliferation, which can be pharmacologically targeted by Cu-selective chelators or activated by ionophores as a target for cancer therapy.<sup>28</sup> However, the design of new molecules capable of chelating intracellular Cu<sup>+</sup> is extremely challenging as Cu<sup>+</sup> binding affinity in the femtomolar range is required to effectively interfere with chaperone/co-chaperone Cu<sup>+</sup> binding.<sup>15</sup>

Using the conserved **MT/CGGC** motif of Cu<sup>+</sup> chaperones, we propose that multiple copies of the motif arranged within a superstructure network should exhibit assembly-enhanced affinity for Cu<sup>+</sup> (Figure 1). Hence, we designed the self-assembling peptide amphiphile **Nap-FFMTCGGCR** comprising three motifs, (1) the naphthalene (**Nap**) capped diphenylalanine (**FF**) domain that promotes self-assembly, (2) the sequence **MT/CGGC** binding Cu<sup>+</sup> with high affinity and selectivity for Cu<sup>+</sup> *versus* other cations, and (3) the arginine (**R**) residue to enhance cellular uptake. Upon internalization, the local enrichment<sup>29</sup> promotes the assembly into cytosolic **Nap-FFMTCGGCR** fibers where they can bind and competitively acquire Cu<sup>+</sup> from the intracellular proteins, ligands, or pools, which induces cellular dysfunctions leading to apoptosis (Figure 1B). Control peptides that cannot self-assemble underline the importance of fibril formation to achieve the desired function. Selectivity towards Cu-sensitive cancer cells such as triple negative breast cancer cells, MDA-MB-231, has been investigated and compared against normal HEK 293T cells. We show that in-situ assembly strategies can be used as a powerful tool to enhance biochemical properties, promoting a collective function that is unavailable in the molecular form.

## **Result and Discussion**

### **Design, synthesis, and Cu<sup>+</sup> binding of Nap-FFMTCGGCR**

Derived from the natural Cu<sup>+</sup> chaperones, the sequence **MTCGGC** is designed featuring two cysteine residues spaced by two glycine residues, responsible for Cu<sup>+</sup> binding. The *N*-terminus of **MTCGGC** is modified with a naphthalene-capped diphenylalanine (**Nap-FF**), that provides hydrophobicity and  $\pi$ - $\pi$  interactions to promote self-assembly into nanofibers. The *C*-terminus is extended with an arginine (**R**) to facilitate cell membrane interactions and cellular uptake. The **FFMTCGGCR** sequence was synthesized using fluorenylmethoxycarbonyl (Fmoc) solid phase peptide synthesis (SPPS) on rink amide resin. The *N*-terminus of the peptide was coupled to naphthalene acetic acid using 2-(1H-benzotriazole-1-yl)-1,1,3,3-tetramethyluronium hexafluorophosphate (HBTU)/N, N-*diisopropylethylamine* (DIPEA) on resin (Figure S1). The **Nap-FFMTCGGCR** was removed from the solid support using a cleavage cocktail based on trifluoroacetic acid (TFA). The cleaved peptide was purified using high-performance liquid chromatography (HPLC) and characterized by electron spray ionization-mass spectrometry (ESI-MS) (Figure S2), <sup>1</sup>H NMR (Figure S3) and <sup>1</sup>H, <sup>1</sup>H-COSY NMR spectroscopy (Figure S4).

**Nap-FFMTCGGCR<sup>mn</sup>** (The superscript “*mn*” represents the monomeric form of the peptide) can be dissolved in solvents including DMSO, methanol, and water/acetonitrile mixture. Its critical aggregation concentration (CAC) in Milli-Q water is 50  $\mu$ M as measured using Nile red (Figure

S5). The predominant oxidation state of Cu inside the cell is +1 due to the reductive intracellular environment,<sup>30</sup> hence we used Cu<sup>+</sup> throughout our investigation from the source Cu<sup>I</sup>[(CH<sub>3</sub>CN)<sub>4</sub>]PF<sub>6</sub>.<sup>31</sup> At first, we studied the Cu<sup>+</sup> binding of **Nap-FFMTCGGCR<sup>mn</sup>** at the molecular level. The **Nap-FFMTCGGCR<sup>mn</sup>** absorbs light at 254-300 nm, which showed an increase in the intensity upon the mol. equivalent addition of Cu<sup>+</sup> (Figure 2A). The Cu<sup>+</sup> bound fraction of **Nap-FFMTCGGCR<sup>mn</sup>** calculated from the UV-Vis spectra suggests 1:1 stoichiometric binding of **Nap-FFMTCGGCR<sup>mn</sup>** to Cu<sup>+</sup> (Table S1). The molecular mass analysis by MALDI-TOF further supported the formation of **Cu<sup>I</sup>-Nap-FFMTCGGCR<sup>mn</sup>** with the appearance of respective molecular mass at 1248.4 (m/z), matching the calculated mass of the Cu<sup>+</sup> bound peptide (Figure S6).

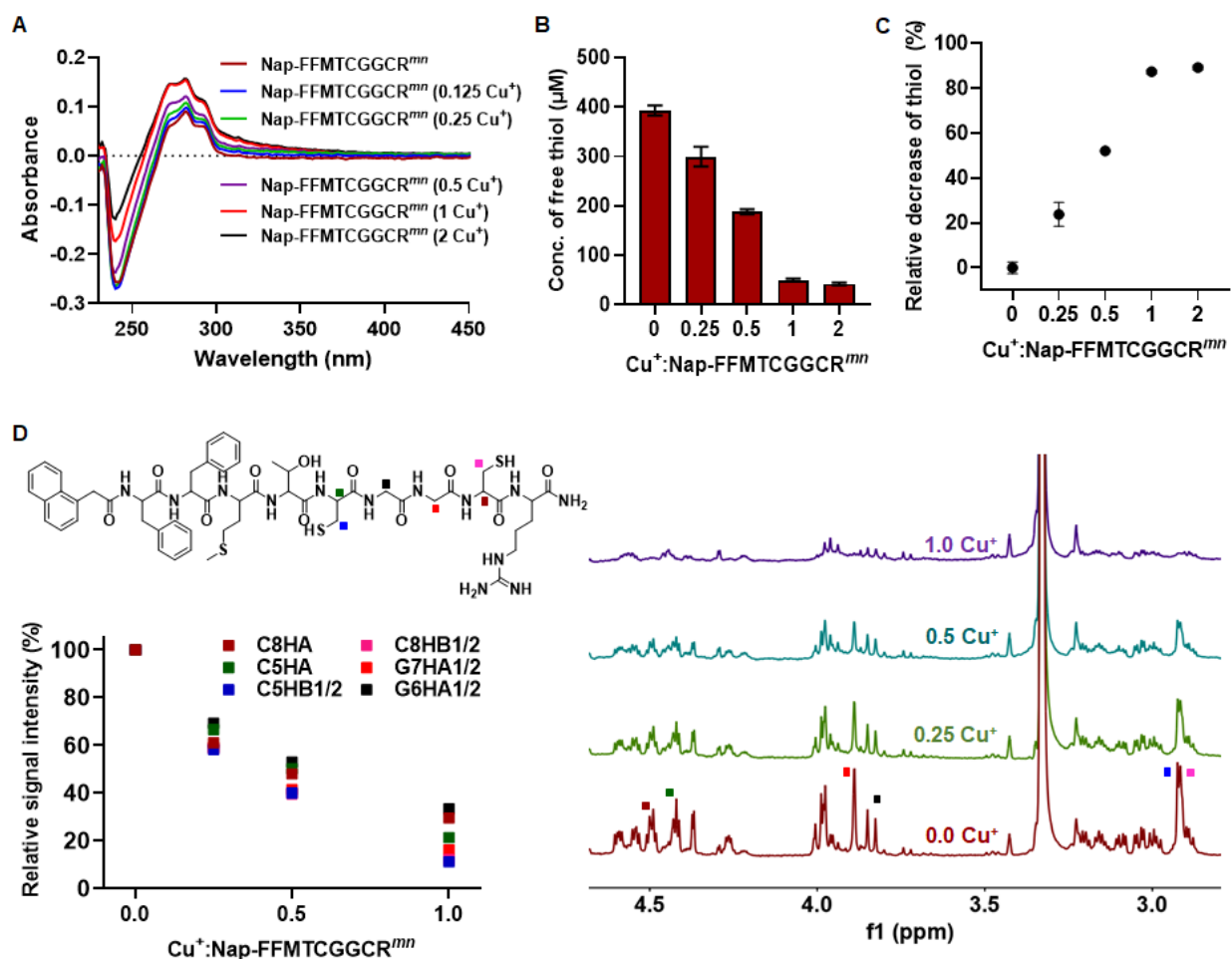


**Figure 2:** A) The UV-Vis spectra of **Nap-FFMTCGGCR<sup>mn</sup>** (20 μM, MeOH) in response to the addition of Cu<sup>+</sup> (0, 0.25, 0.5, 1 and 2 mol. equivalent). B) Ellman's reagent assay showing the decrease of free -SH concentration upon the addition of Cu<sup>+</sup> (0, 0.25, 0.5, 1 and 2 mol. equivalent) to **Nap-FFMTCGGCR<sup>mn</sup>** (MeOH, 400 μM). C) Relative decrease of free -SH concentration calculated from Figure B. D) Relative signal intensity obtained after the addition of Cu<sup>+</sup> (0, 0.25, 0.5 and 1 mol. equivalent) to **Nap-FFMTCGGCR<sup>mn</sup>** calculated from the <sup>1</sup>H NMR spectra (700 MHz, 298 K, MeOH-d<sub>4</sub>) with respect to an internal standard (C<sub>2</sub>H<sub>2</sub>Cl<sub>4</sub>). Corresponding <sup>1</sup>H NMR

spectra (zoom in) and protons of interests are shown. The data represented as mean  $\pm$  s.d.,  $n=3$  for B, C and D.

The Ellman's reagent (5, 5'-dithiobis (2-nitrobenzoic acid), DTNB) assay was conducted to investigate the involvement of sulfhydryl (-SH) functional groups of **Nap-FFMTCGGCR<sup>mn</sup>** on binding to Cu<sup>+</sup>.<sup>32</sup> DTNB reacts with free -SH to produce a mixed disulfide and 2-nitro-5-thiobenzoic acid (TNB). TNB absorbs at 412 nm allowing free -SH groups to be determined quantitatively. Stoichiometric addition of Cu<sup>+</sup> to **Nap-FFMTCGGCR<sup>mn</sup>** caused a decrease in the free -SH concentration of **Nap-FFMTCGGCR<sup>mn</sup>** in which 23.8  $\pm$  5.3 %, 52.1  $\pm$  1.4 %, 87.3  $\pm$  0.89 % and 89.2  $\pm$  0.98 % decrease was observed at 0.25, 0.5, 1 and 2 mol. equivalent addition of Cu<sup>+</sup> respectively (Figure 2B-C, Figure S7). These results reveal the involvement of -SH functional group on binding to Cu<sup>+</sup>.

Next, we analyzed Cu<sup>+</sup> binding of **Nap-FFMTCGGCR<sup>mn</sup>** by <sup>1</sup>H NMR. First, the structure of **Nap-FFMTCGGCR<sup>mn</sup>** was characterized by <sup>1</sup>H NMR in DMSO-d<sub>6</sub> as the solvent, as depicted in Figure S3. Next, Cu<sup>+</sup> binding to **Nap-FFMTCGGCR<sup>mn</sup>** was studied by <sup>1</sup>H NMR in MeOH-d<sub>4</sub>, which was necessary to prevent oxidation of the peptide. We observed a progressive loss of <sup>1</sup>H NMR signal intensity upon the stoichiometric addition of Cu<sup>+</sup> to **Nap-FFMTCGGCR<sup>mn</sup>** accompanied by broadening of the peaks as depicted in Figure S8. This observation supports binding of Cu<sup>+</sup> to **Nap-FFMTCGGCR<sup>mn</sup>**.<sup>33</sup> Quantitative NMR analysis of the signal intensity with respect to the internal standard C<sub>2</sub>H<sub>2</sub>Cl<sub>4</sub> (at 6.49 ppm) was performed and the results were summarized in Figure S9 and Figure 2D. Upon the addition of 0.5 mol. equivalent Cu<sup>+</sup>, the signal intensity of protons C5HA (4.43 ppm), C5HB1/2 (2.9 ppm), C8HA(4.49 ppm), C8HB1/2 (2.89 ppm), G6HA1/2 (3.84 ppm) and G7HA1/2 (3.9 ppm) decreased, from 100 % without Cu<sup>+</sup>, to 46.0  $\pm$  0.23 %, 37.3  $\pm$  0.08 %, 44.3  $\pm$  0.3 %, 36.8  $\pm$  0.1 %, 48.4  $\pm$  0.3 % and 38.3  $\pm$  0.2 %, respectively. Upon addition of one mol. equivalent Cu<sup>+</sup>, the signal intensity of the respective protons further decreased to 23.5  $\pm$  0.5 %, 9.9  $\pm$  0.2 %, 14.5  $\pm$  0.3 %, 10.7  $\pm$  0.2 %, 30.1  $\pm$  0.3 %, 11.3  $\pm$  0.3 %. These results support that the **CGGC** motif was likely involved in binding to Cu<sup>+</sup>. In particular, the signal intensities of the  $\beta$ -protons of the Cys residues were reduced significantly after the addition of equimolar Cu<sup>+</sup> (Figure 2D), whereas the signal intensities of the aromatic protons (i.e. F2HD1/2 at 7.0 ppm, 39.4  $\pm$  0.2 %) were less affected (Figure S10). Furthermore, their integrals did not show any obvious changes with respect to the reference, suggesting that no aggregation occurred within the tested period of up to 24 h (Figure S11). From these observations, we suggest that Cu<sup>+</sup> binding to **Nap-FFMTCGGCR<sup>mn</sup>** should result in a restricted mobility of **Nap-FFMTCGGCR<sup>mn</sup>** leading to the loss of proton signals. Further, the EPR spectra showed no signal corresponding to Cu<sup>2+</sup> indicating the stability of Cu<sup>+</sup> upon binding to **Nap-FFMTCGGCR<sup>mn</sup>** within 24 h (Figure S12). Cu<sup>+</sup> binding to **Nap-FFMTCGGCR<sup>mn</sup>** in aqueous conditions was further supported by monitoring the UV-Vis spectra in Milli-Q water, which showed a similar trend as observed in the case of MeOH (Figure S13). The **Nap-FFMTCGGCR<sup>mn</sup>** peptide showed high specificity towards Cu<sup>+</sup> and no obvious response to other physiologically relevant metal ions such as K<sup>+</sup>, Ca<sup>2+</sup>, Zn<sup>2+</sup>, Co<sup>2+</sup>, Fe<sup>2+</sup>, and Mg<sup>2+</sup> was observed, except towards Cu<sup>2+</sup> (Figure S14).

## Nap-FFMTCGGCR<sup>ag</sup> efficiently bind Cu<sup>+</sup>

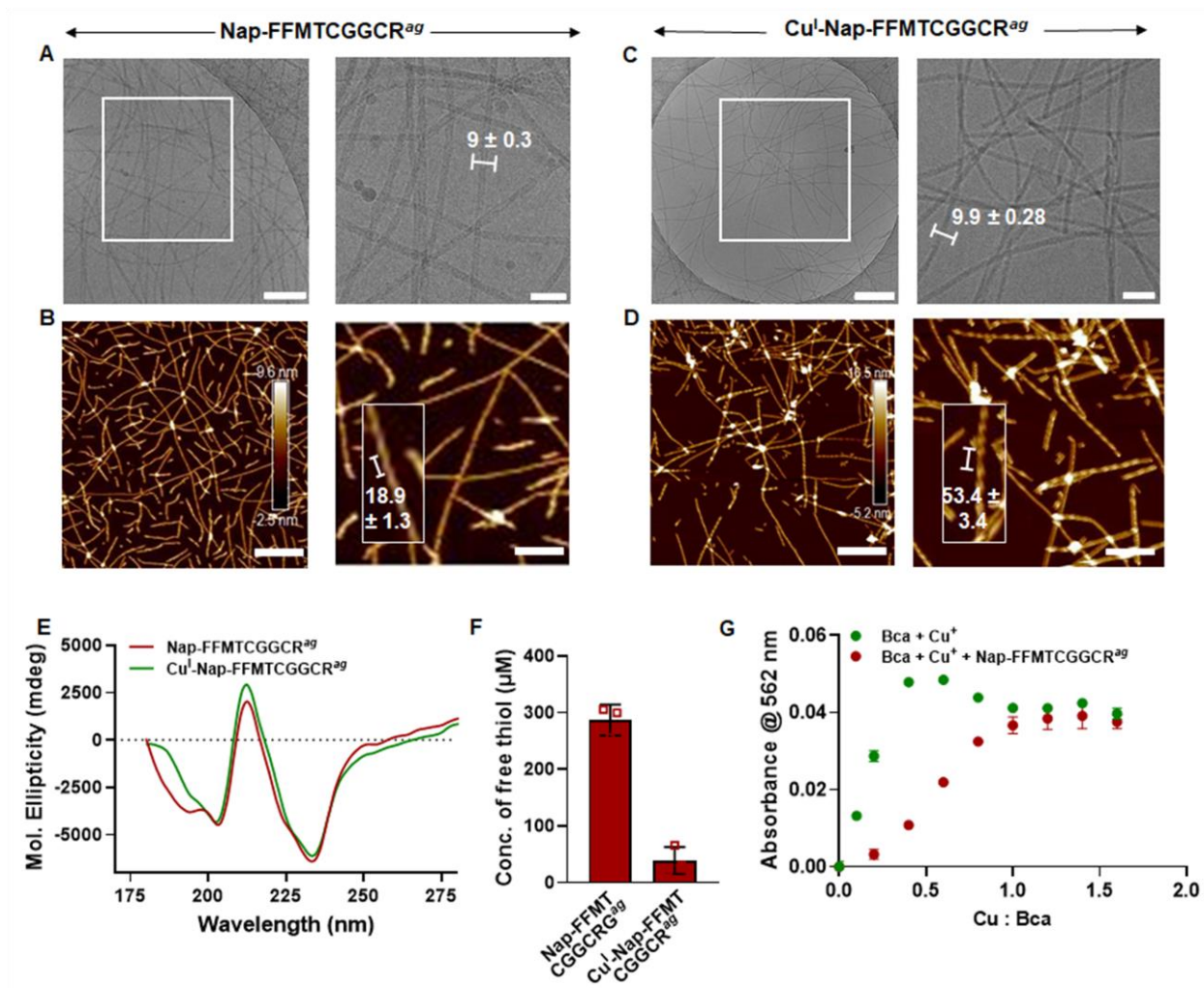


**Figure 3:** The microscopic images of A) **Nap-FFMTCGGCR<sup>ag</sup>** (100 μM, Milli-Q) observed under Cryo-EM (scale bar: 200 nm and 50 nm respectively) and B) Liquid tapping AFM (Scale bar: 270 nm and 100 nm respectively). The microscopic images of **Cu<sup>I</sup>-Nap-FFMTCGGCR<sup>ag</sup>** (100 μM, Milli-Q) observed under C) Cryo-EM (Scale bar: 200 nm and 50 nm respectively) and D) Liquid tapping AFM (Scale bar: 600 nm and 280 nm respectively). E) CD spectra of **Nap-FFMTCGGCR<sup>ag</sup>** (100 μM) and **Cu<sup>I</sup>-Nap-FFMTCGGCR<sup>ag</sup>** (1:1, 100 μM). F) The Ellman's reagent assay showing 80 % reduction in the surface thiols of **Nap-FFMTCGGCR<sup>ag</sup>** (100 μM) after adding 1 mol. equivalent of Cu<sup>+</sup>. G) The binding titration curve of **Nap-FFMTCGGCR<sup>ag</sup>** (100 μM) and Bca (100 μM) towards Cu<sup>+</sup> (0-160 μM). The data represented as mean ± s.d.,  $n=3$ . The diameter of individual fibers was obtained from TEM images measured using Image J data processing software. The data represented as mean ± s.d.,  $n=100$ . The helical length was obtained from AFM images measured using NanoScope Analysis data processing software. The data represented as mean ± s.d.,  $n=5$ .

Next, we studied  $\text{Cu}^+$  binding to **Nap-FFMTCGGCR<sup>ag</sup>** (the superscript “ag” refers to peptides in their aggregated state) above the CAC of 50  $\mu\text{M}$  in Milli-Q water. The CAC remained unchanged after the addition of  $\text{Cu}^+$  (1 mol. equivalent) as shown in Figure S15. Cryo electron microscopy (Cryo-EM) showed that **Nap-FFMTCGGCR<sup>ag</sup>** self-assembled into ordered nanofibers of  $9 \pm 0.3$  nm diameter and several micrometers in length (Figure 3A, Figure S16) that slightly increased to  $9.9 \pm 0.3$  nm after binding to  $\text{Cu}^+$  (Figure 3C, Figure S17). Liquid-tapping atomic force microscopy (AFM) showed that the **Nap-FFMTCGGCR<sup>ag</sup>** fibers are helical with a helical distance of  $18.9 \pm 1.3$  nm that increased to  $53.4 \pm 3.4$  nm after binding to  $\text{Cu}^+$  (Figure 3B, 3D, Figure S18-19). The UV-Vis spectra revealed an increase in the absorption at 254-300 nm after binding to  $\text{Cu}^+$  (Figure S20). The secondary structure conformation of the **Nap-FFMTCGGCR<sup>ag</sup>** was assessed using circular dichroism (CD) spectroscopy. The spectra showed a strong negative cotton effect at 233 nm, a positive cotton effect at 212 nm, and a negative cotton effect at 203 nm indicating the presence of cation- $\pi$  interactions,  $\beta$ -sheets, and  $\alpha$ -helix conformation respectively, which are retained after binding to equimolar  $\text{Cu}^+$  (Figure 3E). These observations suggest that the morphology of **Nap-FFMTCGGCR<sup>ag</sup>** nanofibers did not alter after binding to  $\text{Cu}^+$ .<sup>34-35</sup>

Ellman’s reagent assay showed 80 % decrease in the free thiols of the **Nap-FFMTCGGCR<sup>ag</sup>** upon binding to 1 mol. equivalent  $\text{Cu}^+$  (Figure 3F, Figure S21). The surface charge distribution of **Nap-FFMTCGGCR<sup>ag</sup>** showed an average zeta potential of  $46 \pm 2.2$  mV (100  $\mu\text{M}$ ), which remained unchanged ( $46.9 \pm 2$  mV, Figure S22) after  $\text{Cu}^+$  binding (1:1). A 1:1 binding stoichiometry of **Nap-FFMTCGGCR<sup>ag</sup>** to  $\text{Cu}^+$  was observed in a titration experiment using the known  $\text{Cu}^+$  chelator bicinchoninate (Bca) (Figure S23)<sup>36</sup>. Bca binds  $\text{Cu}^+$  with a 2:1 (Bca :  $\text{Cu}^+$ ) stoichiometric ratio forming a pink-colored complex of  $[\text{Cu}^{\text{I}}(\text{Bca})_2]^{3-}$  that absorbs at 562 nm. Titration of  $\text{Cu}^+$  (0-160  $\mu\text{M}$ ) and 100  $\mu\text{M}$  of Bca showed a linear increase in the absorbance at 562 nm reaching a maximum upon the addition of  $\sim 0.5$  equivalent (50  $\mu\text{M}$ ) of  $\text{Cu}^+$  corresponding to the formation of  $[\text{Cu}^{\text{I}}(\text{Bca})_2]^{3-}$ . However, the similar titration into the solution containing the mixture of Bca (100  $\mu\text{M}$ ) and **Nap-FFMTCGGCR<sup>ag</sup>** (100  $\mu\text{M}$ ) showed a delayed increase in the absorbance at 562 nm, requiring  $\sim 140$   $\mu\text{M}$  of  $\text{Cu}^+$  to reach the plateau (Figure 3G). The titration curve indicates that the **Nap-FFMTCGGCR<sup>ag</sup>** binds  $\text{Cu}^+$  with a stoichiometry of nearly 1:1. Additionally, these results indicate that **Nap-FFMTCGGCR<sup>ag</sup>** binds  $\text{Cu}^+$  even in the presence of Bca. Bca binds  $\text{Cu}^+$  with a high binding constant of  $10^{17.3} \text{ M}^{-2}$  as reported previously<sup>36-37</sup>, which allowed us to estimate the dissociation constant of **Nap-FFMTCGGCR<sup>ag</sup>** with bound  $\text{Cu}^+$  in a competitive binding titration experiment with Bca. A very low  $K_D$  of  $(2.3 \pm 1.6) \times 10^{-14.3} \text{ M}^{36}$  was observed for **Nap-FFMTCGGCR<sup>ag</sup>** with  $\text{Cu}^+$  (Table S2).

### **Intracellular self-assembly of Nap-FFMTCGGCR.**

Triple negative MDA-MB-231 breast cancer cells have a high demand for  $\text{Cu}^+$  compared to healthy cells<sup>38</sup>, which is supported by the upregulation of mitochondrial  $\text{Cu}^+$  chaperone/co-chaperone proteins COX17 and Sco2.<sup>39</sup> To image the internalization and intracellular self-assembly of **Nap-FFMTCGGCR** in MDA-MB-231 cells by fluorescence microscopy, the fluorescent peptide derivative **NBD-FFMTCGGCR** was synthesized by replacing naphthalene with 4-nitro-2, 1, 3-benzoxadiazole (NBD) (Figure S24). The NBD fluorophore has been used before for imaging *in cellulo* self-assembled nanofibers (Figure 4A).<sup>40</sup> **NBD-FFMTCGGCR** and **Nap-FFMTCGGCR**

co-assemble into nanofibers with an average diameter of  $12.47 \pm 0.7$  nm (Figure S25). These co-assembled fibers absorb light at 480 nm ( $\lambda_{max}$ ) and emit at 550 nm ( $\lambda_{max}$ ) as depicted in Figure S26, rendering them suitable for visualization under confocal microscopy. Notably, **NBD-FFMTCGGCR** itself does not self-assemble into nanofibers at 100  $\mu$ M (Figure S27). The MDA-MB-231 cells were incubated with a mixture of **NBD-FFMTCGGCR** and **Nap-FFMTCGGCR** (5  $\mu$ M each, 10  $\mu$ M total), which forms co-aggregates inside the cells, and were visualized by confocal microscopy after 24 h. A bright green fluorescence was observed from the cell confirming cellular internalization (Figure 4B) and intracellular nanofiber formation of **Nap/NBD-FFMTCGGCR<sup>ag</sup>** via co-assembly as shown in Figure 4A. In contrast, **NBD-FFMTCGGCR** (10  $\mu$ M) did not form any aggregates inside cells, most likely due to the higher CAC of NBD versus Nap (Figure 4C).<sup>41</sup>

Next, holotomographic microscopy was applied to study the label-free assembly of **Nap-FFMTCGGCR** inside the cell. Holotomographic microscopy measures the refractive indices of the cellular compartments to create a holotomogram. The peptides that aggregated or self-assembled into nanofibers possess refractive indices ( $\sim 1.35$ - $1.36$ ) measurable by a holotomography. First, the holotomogram of untreated MDA-MB-231 cells was taken as shown in Figure 4D. The refractive indices of the cellular components such as nucleoli, lipid droplets and mitochondria were measured approximately as  $1.349 \pm 0.0043$ ,  $1.366 \pm 0.0016$  and  $1.342 \pm 0.0014$ , respectively (in DMEM medium). Incubating MDA-MB-231 cells with **Nap-FFMTCGGCR** (10 or 20  $\mu$ M) showed the presence of aggregates inside the cell possessing a refractive index of  $1.357 \pm 0.004$  (Figure 4E, Figure S28), which can be visually distinguished from lipid droplets. To differentiate the **Nap-FFMTCGGCR<sup>ag</sup>** from lipid droplets within the cell using fluorescence, **Nap/NBD-FFMTCGGCR** were co-assembled inside the cells. **NBD-FFMTCGGCR** (10  $\mu$ M) itself does not form aggregates in cells and therefore, no fluorescence signals were observed under holotomography as depicted in Figure S29A, which is consistent with the confocal images. However, after incubation of both **Nap/NBD-FFMTCGGCR** (10  $\mu$ M), intracellular aggregates were detected by their green fluorescence suggesting that co-incubation results in the formation of **Nap/NBD-FFMTCGGCR<sup>ag</sup>** inside the cell (Figure S29B). Notably, 10  $\mu$ M of **Nap/NBD-FFMTCGGCR** does not self-assemble into nanofibers outside of the cell, underscoring the significance of intracellular enrichment of both peptides to self-assemble into structures inside the cell when incubated at 10  $\mu$ M (Figure S30). We have performed the segmentation of **Nap/NBD-FFMTCGGCR<sup>ag</sup>** and lipid droplets as shown in Figure 4F. The lipid droplets were present in the untreated control cells, as well as in the **NBD-FFMTCGGCR** and **Nap/NBD-FFMTCGGCR** treated cells while peptide aggregates were present only in **Nap/NBD-FFMTCGGCR** treated cells (Figure 4F, Figure S31). The lipid droplets and aggregates showed no co-localization (Figure S32). To verify whether the co-assembled structures were localized in any subcellular compartment, cellular co-localization analysis was conducted. MDA-MB-231 cells were incubated with **Nap/NBD-FFMTCGGCR** (10  $\mu$ M) for 12 h before imaging by confocal microscopy. No co-localization was found with mitochondria (MitoTracker™ Red FM) nor with the endoplasmic reticulum (ER-Tracker™ Red). Partial co-localization with endo-lysosomes (LysoTracker™ Red) (Pearson coefficient 0.31) suggests that the peptides likely internalize *via* endocytosis (Figure S33-S35).

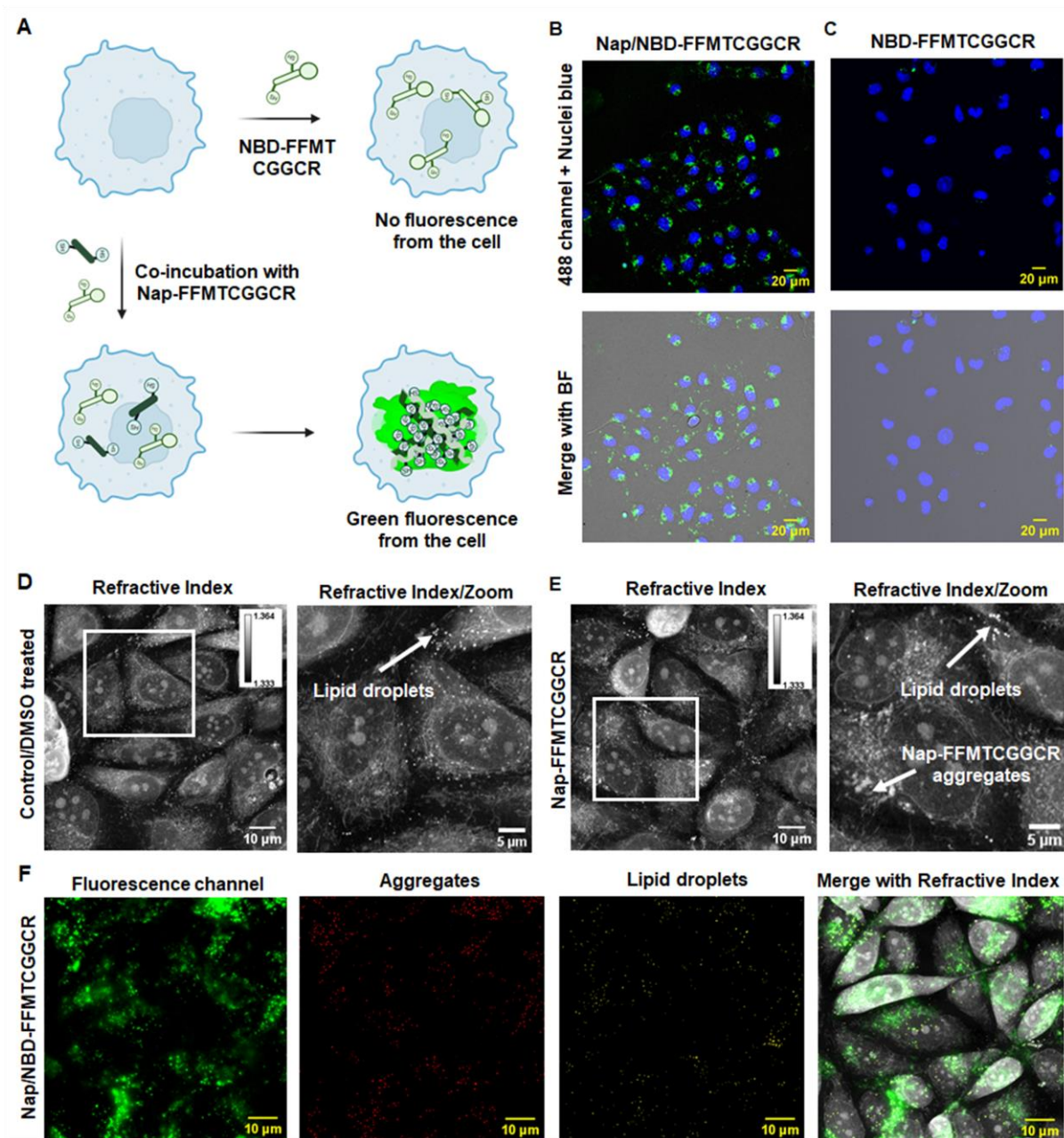


**Figure 4:** A) Schematic illustration of co-assembly approach to study the self-assembly of **Nap-FFMTCGGCR** inside the cell. Confocal microscopy images of MDA-MB-231 cells treated with B) **NBD/Nap-FFMTCGGCR** (10 μM) and C) **NBD-FFMTCGGCR** (10 μM) imaged after 24 h of incubation. The nuclei were labelled with NucBlue™. Holotomogram of D) control (treated with DMSO) MDA-MB-231 cells. The calibration bar indicates the refractive index (RI). The lipid droplets are marked with arrows, and E) MDA-MB-231 cells treated with **Nap-FFMTCGGCR** imaged after 24 h showing the presence of aggregates of RI  $\sim 1.357 \pm 0.004$ . F) The segmented holotomogram of MDA-MB-231 treated with **Nap/NBD-FFMTCGGCR** showing the appearance of green fluorescence corresponding to the aggregates. The yellow dots indicate lipid droplets and red dots indicate aggregates formed inside the cell upon treatment with **Nap/NBD-FFMTCGGCR**. The segmentation was performed using random forest-based pixel classification.

### **Nap-FFMTCGGCR induces cancer cell apoptosis.**

The analysis of breast cancer data from the cancer genome atlas (TCDA) unveiled a noteworthy upregulation of 26 % of the copper proteome proteins.<sup>42</sup> Notable among these proteins are F5, ATP7B, SLC31A1, SCO2, HEPHL1, CUTA, ATOX1, COX17, TYRP1, MT3, LOX-like protein 1 and 2, SPARC, and MOXD1.<sup>42-43</sup> Several factors may contribute to this heightened demand compared to normal cells, with a primary consideration being the pivotal role of Cu<sup>+</sup> as a cofactor for complex IV (COX17) within the mitochondrial electron transport chain. Complex IV is responsible for energy production and serves as a crucial component of oxidative phosphorylation (OXPHOS). Since breast cancer metabolism relies on OXPHOS, any impairment in Cu<sup>+</sup> trafficking is anticipated to have deleterious effects. We envisaged that the binding of Cu<sup>+</sup> by *in cellulo* self-assembled **Nap-FFMTCGGC<sup>ag</sup>** could interrupt Cu<sup>+</sup> homeostasis and adversely affect the growth of breast cancer cells that require Cu<sup>+</sup> for growth and proliferation. At first, we examined the survival rate of MDA-MB-231 breast cancer cells after treating them with **Nap-FFMTCGGCR** in a time-dependent manner. MDA-MB-231 cells were incubated with 10 μM of **Nap-FFMTCGGCR** to analyze the cell survival over time. For an incubation time of 24 h with **Nap-FFMTCGGCR**, 78.8 ± 8.8% viable cells were detected. After 48 and 72 h, the cell survival rate was further reduced to 39.2 ± 4.5% and 14.2 ± 2.9%, respectively, suggesting that treatment with **Nap-FFMTCGGCR** effectively reduced the viability of MDA-MB-231 breast cancer cells over time (Figure 5A).

However, the observed reduction in cell viability could either originate from **Nap-FFMTCGGC<sup>ag</sup>** formed inside the cell or from a synergistic effect arising from both aggregation and the disruption of Cu<sup>+</sup> homeostasis. Therefore, the control peptide, **Nap-FFMTGGR**, that also self-assembles (CAC: 45 μM in Milli-Q water) but does not bind Cu<sup>+</sup> due to the absence of the Cys residues was synthesized (Figure S36-38). First, fiber formation of **Nap-FFMTGGR<sup>ag</sup>** was assessed outside cells and fibers with diameter 5.9 ± 0.3 nm were obtained (Figure S39). Next, the impact of *in cellulo* aggregation of **Nap-FFMTGGR** (10 μM incubation) on the cell viability was tested. However, cells remained viable even after 48 h, and only after 72 h, the cell viability decreased to 55.7 ± 2.9 % (Figure 5B). This observation suggests, the peptide aggregates, devoid of Cu<sup>+</sup>-binding motif required significantly longer incubation time to induce cytotoxic effects on MDA-MB-231 cells. Concentration-dependent cell viability analysis of both **Nap-FFMTCGGCR** and **Nap-FFMTGGR** was performed on MDA-MB-231 cells (48 h incubation) showed that **Nap-FFMTCGGCR** induced cytotoxicity with an IC<sub>50</sub> of 6.5 μM while **Nap-FFMTGGR** showed an approximate 3-fold higher IC<sub>50</sub> of 19.9 μM (Figure 5C). Interestingly, both compounds did not exhibit any cytotoxicity in normal HEK 293 T cells at the tested conditions (48 h, up to 20 μM) indicating pronounced cytotoxicity in cancer versus healthy cells (Figure 5D). The apoptosis assay monitored by FITC-Annexin V and propidium iodide (PI) showed Annexin V staining on the plasma membrane of the MDA-MB-231 cells treated by **Nap-FFMTCGGCR**, indicating that the cells initiated early apoptotic pathways after 48 h (10 μM) of incubation (Figure 5E). Notably, the absence of PI signal indicates that cell death was primarily caused by apoptosis. In contrast, **Nap-FFMTGGR** did not induce apoptosis under this condition 48 h (10 μM) (Figure 5F).

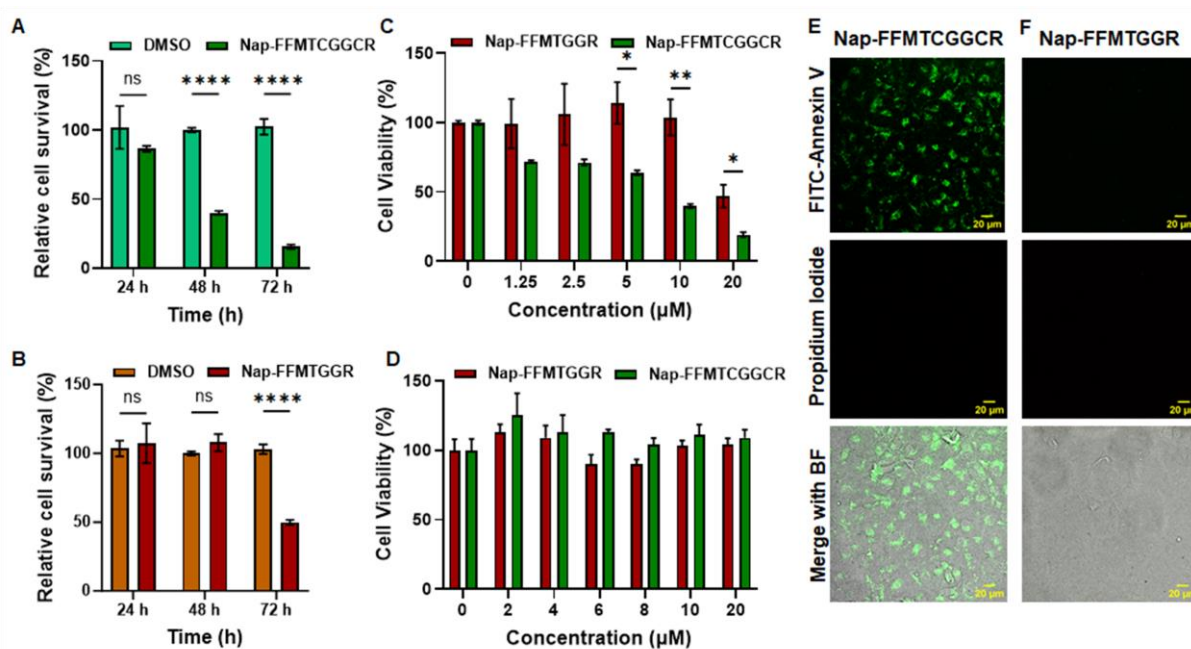


**Figure 5:** The response of MDA-MB-231 cells towards the treatment with A) **Nap-FFMTCGGCR** (10 μM) and B) **Nap-FFMTGGR** (10 μM) over time. Dose-dependent cell viability analysis of **Nap-FFMTCGGCR** and **Nap-FFMTGGR** towards C) MDA-MB-231 cells and D) HEK 239T cells analyzed after 48 h. Live/dead cell assay performed using FITC-Annexin V/Propidium Iodide staining after treating with E) **Nap-FFMTCGGCR** (10 μM, 48 h) and F) **Nap-FFMTGGR** (10 μM, 48 h). Statistical analysis was performed using unpaired t-test corrected for Bonferroni-Dunn method, set P value threshold 0.05, 0.1234 (ns), \*\* $P < 0.0332$ , \*\* $P < 0.0021$ , \*\*\* $P < 0.0002$ , \*\*\*\* $P < 0.0001$ ). The data represented as mean  $\pm$  s.d.,  $n=3$ .

### **Nap-FFMTCGGCR interrupt $\text{Cu}^+$ homeostasis and induces oxidative stress to cancer cells.**

Next, we investigated the underlying mechanisms leading to the cell toxicity upon treatment with **Nap-FFMTCGGCR**. We assume that the high affinity of **Nap-FFMTCGGCR<sup>ag</sup>** towards  $\text{Cu}^+$  possibly enables them to successfully compete with cytosolic  $\text{Cu}^+$  chaperones or intracellular  $\text{Cu}^+$ -complexes.  $\text{Cu}^+$  homeostasis is strongly correlated with the redox balance of the cell because superoxide dismutase1 (SOD1), the key enzyme responsible for the redox balance of the cell, uses  $\text{Cu}^+$  as the cofactor.<sup>44</sup> SOD1 is an antioxidant enzyme that scavenges the superoxide anion by converting the free radical to oxygen and hydrogen peroxide.<sup>45</sup> We postulates that the  $\text{Cu}^+$  binding ability of **Nap-FFMTCGGCR<sup>ag</sup>** could induce  $\text{Cu}^+$  starvation of SOD1 enzyme, causing redox imbalance within the cell. First, we studied whether the SOD1 activity of the cells was affected upon treatment with **Nap-FFMTCGGCR**. The cellular SOD1 activity of the untreated control cell group was measured as  $0.404 \pm 0.01$  U/mL. After treating with **Nap-FFMTCGGCR** for 48 h (20 μM), there was 8-fold reduction in activity ( $0.05 \pm 0.00345$  U/mL). In contrast, treatment with **Nap-FFMTGGR** showed no noticeable changes ( $0.43 \pm 0.02$  U/mL) relative to the untreated control group (Figure 6A, Figure S40). We anticipate that **Nap-FFMTCGGCR<sup>ag</sup>** formed within

the cell could potentially interact with CCS chaperone, thereby interrupting the delivery of  $\text{Cu}^+$  to SOD1. SOD1 is the counter chaperone for CCS. Given that  $\text{Cu}^+$  serves as a cofactor for the proper functioning of SOD1, inadequate  $\text{Cu}^+$  likely leads to a loss of SOD1 activity.

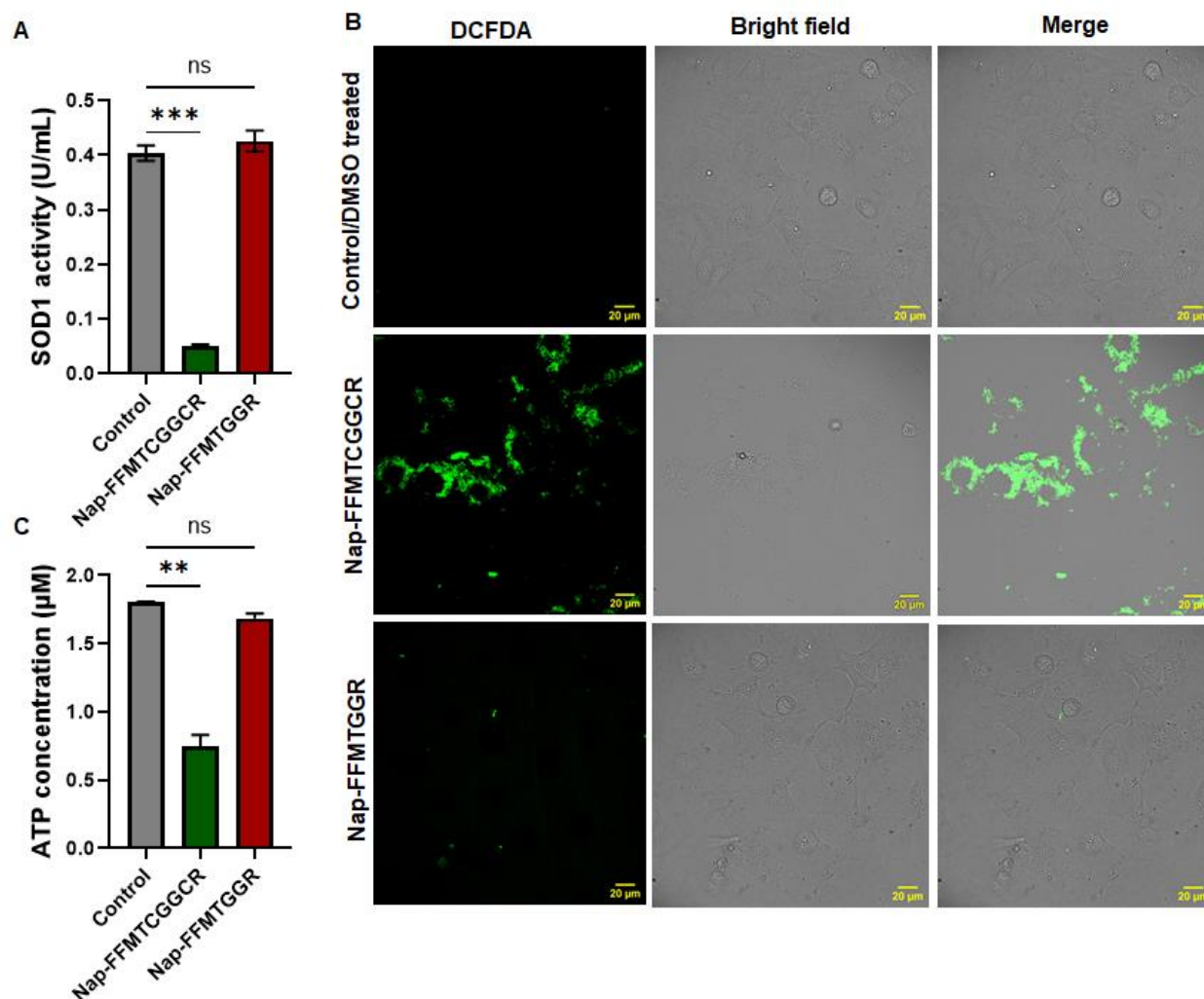


**Figure 6:** A) SOD1 analysis of MDA-MB-231 cells after treating with **Nap-FFMTCGGCR** or **Nap-FFMTGGR** (20  $\mu\text{M}$ , 48 h). B) ROS generation inside the MDA-MB-231 cells measured using DCFDA probe after treating with **Nap-FFMTCGGCR** or **Nap-FFMTGGR** (20  $\mu\text{M}$ , 48 h), C) ATP concentration of MDA-MB-231 cells after treating with **Nap-FFMTCGGCR** or **Nap-FFMTCGGCR** (10  $\mu\text{M}$ , 72 h). The error bars represent standard deviation from three replicate sample measurements. Statistical analysis was performed using one-way ANOVA (corrected for Bonferroni method). *P* values: 0.12 (ns), 0.033 (\*), 0.002 (\*\*), <0.001 (\*\*\*). The data represented as mean  $\pm$  s.d.,  $n=3$ .

Subsequently, we explored whether the reduced SOD1 activity contributes to elevated cellular oxidative stress level using an assay based on 2',7'-dichlorofluorescein diacetate (DCFDA) probe. DCFDA is a cell-permeable fluorogenic dye that measures the activity of reactive oxygen species (ROS) such as hydroxyl, peroxy and singlet oxygen within the cell. MDA-MB-231 cells were

treated with 20  $\mu\text{M}$  of **Nap-FFMTCGGCR** or **Nap-FFMTGGR** for 48 h. Following confocal imaging analysis after staining with the DCFDA probe, bright fluorescence was observed from the cells treated with **Nap-FFMTCGGCR** (Figure 6B). However, **Nap-FFMTGGR** treated cells did not show fluorescence within the tested conditions (20  $\mu\text{M}$ , 48 h). This observation was further validated by flow cytometric analysis (Figure S41). We anticipate that the elevated cellular oxidative stress can induce metabolic defects in cells. To examine whether intracellular aggregation and consequent  $\text{Cu}^+$  binding of **Nap-FFMTCGGCR**<sup>48</sup> induce any metabolic defects, we evaluated cellular ATP levels following treatment with **Nap-FFMTCGGCR** or **Nap-FFMTGGR**. The ATP concentration of the untreated control MDA-MB-231 cell group was measured as  $1.8 \pm 0.006 \mu\text{M}$ . As anticipated, treatment with **Nap-FFMTCGGCR** (20  $\mu\text{M}$ , 48 h) reduced the ATP level to  $0.74 \pm 0.09 \mu\text{M}$ . However, the ATP level in the **Nap-FFMTGGR** treated group showed no significant difference ( $1.68 \pm 0.04 \mu\text{M}$ ) compared to the control group under similar conditions (Figure 6C, Figure S42).

### **Fiber morphology is essential to interrupt intracellular $\text{Cu}^+$ homeostasis.**

To investigate the influence of fiber morphology on the disruption of intracellular  $\text{Cu}^+$  homeostasis, we conducted experiments involving a control peptide, **Nap-MTCGGCR** (Figure S43). **Nap-MTCGGCR** incorporates a  $\text{Cu}^+$ -binding domain without a self-assembly promoter (**Nap-FF**). The  $\text{Cu}^+$  binding of **Nap-MTCGGCR** was validated through UV-Vis spectral analysis, revealing the increase in the absorbance at 254-300 nm upon binding to  $\text{Cu}^+$  (Figure 7A). **Nap-MTCGGCR** showed no self-assembled structures in the TEM when analyzed at 100  $\mu\text{M}$  (Figure 7B, Figure S44). The cytotoxicity analysis performed on MDA-MB-231 cells revealed no adverse effects even at a treatment concentration of 100  $\mu\text{M}$  tested for 72 h. This result suggests that the presence of the  $\text{Cu}^+$ -binding domain at the molecular level alone is insufficient to disrupt the  $\text{Cu}^+$  homeostasis within the cellular environment. In support, the Annexin V/PI staining assay did not exhibit positive staining for either Annexin V or PI following treatment with **Nap-MTCGGCR** (20  $\mu\text{M}$ , 46 h), indicating that **Nap-MTCGGCR** failed to trigger the cell death in MDA-MB-231 cells (Figure S45). These outcomes underscore the significance of intracellular self-assembly in effectively binding and disrupting cellular  $\text{Cu}^+$  homeostasis.

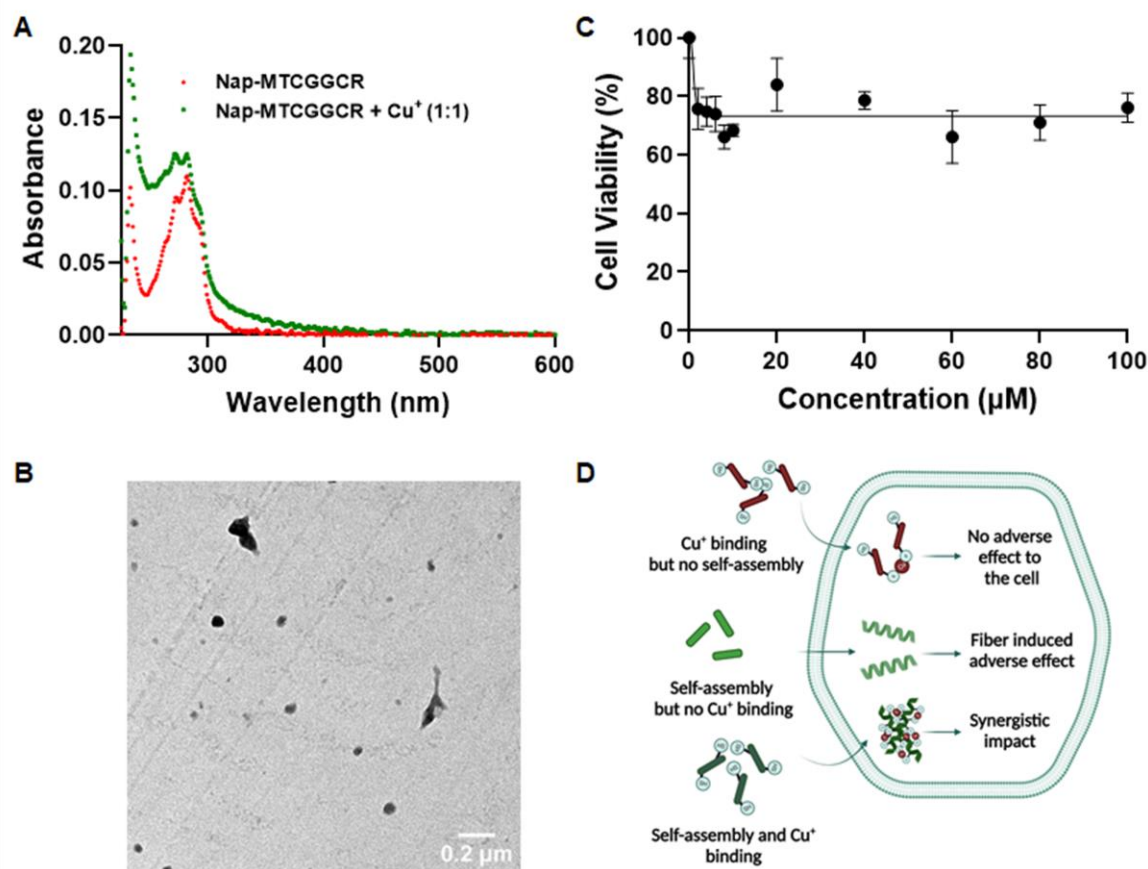


**Figure 7:** A) The UV-Vis spectra of **Nap-MTCGGCR** (40 μM, Milli-Q) in response to the addition of Cu<sup>+</sup> (1 mol. equivalent). B) TEM image of **Nap-MTCGGCR** (100 μM) showing no nanostructure formation. C) Cell viability analysis of **Nap-MTCGGCR** against MDA-MB-231 cells tested for 72 h. D) Schematic illustration of the behavior of **Nap-MTCGGCR**, **Nap-FFMTGGR** and **Nap-FFMTCGGCR** inside a cancer cell. The data represented as mean ± s.d.,  $n=3$  for C.

## Conclusion

While targeting Cu<sup>+</sup> homeostasis has emerged as a promising approach for cancer therapeutics, progress in this field has been limited by the insufficient disruption of Cu<sup>+</sup> homeostasis by small molecules. Inspired by natural Cu<sup>+</sup> chaperones, we amplify the capabilities of Cu<sup>+</sup>-binding motifs using supramolecular concepts to localize a high local concentration of Cu<sup>+</sup>-binding domain onto self-assembled nanostructures within cells. These **Nap-FFMTCGGCR<sup>ag</sup>** structures successfully compete with the natural Cu<sup>+</sup> binding systems in triple negative breast cancer cells (MDA-MB-231), addressing the limitation possessed by small molecules in interrupting Cu<sup>+</sup> homeostasis. We were able to dissect the cellular responses due to Cu<sup>+</sup> binding from those initiated exclusively through fibril formation based on the control peptide **Nap-FFMTGGR** that assembles but does not bind Cu<sup>+</sup>. Moreover, we substantiated that the mere existence of the Cu<sup>+</sup>-binding motif does not ensure the interruption of Cu<sup>+</sup> homeostasis within the cell, as evidenced by the analysis of a non-

assembling control peptide, **Nap-MTCGGCR**. We show that molecular functions combined with in-situ self-assembly technologies is an attractive strategy to amplify their bioactivity in living cells.

### **Author contributions**

J.M.T conceived the idea, designed, and carried out the experiments, analyzed data and wrote the original draft. J.M. T, J. L, R. G and M. W performed NMR experiments and data analysis. J. L. assigned the NMR signals. J. Z performed AFM measurement. I.H performed Cryo-EM measurement with support from I.L and K.L. P.T performed segmentation of hologram. J.M.T and R.G performed ESR measurements. L.A.B and H.R.A.J contributed to the NMR analysis. L. C and J.R provided initial grant support and discussions while J.M.T worked at Stanford University. J.M.T and D.N performed the confocal experiments. T.W. and D.N. supervised the project. T.W. provided the facilities, resources, and revised the manuscript. The final manuscript was approved by all authors.

### **Acknowledgements**

J.M.T is supported by the Alexander von Humboldt Foundation. Support by the IMB Flow Cytometry and Microscopy Core Facility is gratefully acknowledged. I.H. thank the funding support from the H2020 Marie Curie Actions Fellowship of the European Commission (ITN SUPERCOL, grant agreement 860914). J.M.T., L.C., and J.R. acknowledge the grant support by the NCI (R01CA243033).

### **Reference**

1. Liu, Y., Wang, Y., Song, S. & Zhang, H. Cancer therapeutic strategies based on metal ions. *Chem. Sci.* **12**, 12234–12247 (2021).
2. Drażkiewicz, M., Skórzyńska-Polit, E. & Krupa, Z. Copper-induced oxidative stress and antioxidant defence in *Arabidopsis thaliana*. *BioMetals* **17**, 379–387 (2004).
3. Ruiz, L. M., Libedinsky, A. & Elorza, A. A. Role of copper on mitochondrial function and metabolism. *Front. Mol. Biosci.* **8**, 711227 (2021).
4. Dancis, A. *et al.* Molecular characterization of a copper transport protein in *S. cerevisiae*: An unexpected role for copper in iron transport. *Cell* **76**, 393–402 (1994).
5. Wang, J. *et al.* Inhibition of human copper trafficking by a small molecule significantly attenuates cancer cell proliferation. *Nat. Chem.* **7**, 968–979 (2015).
6. Gupte, A. & Mumper, R. J. Elevated copper and oxidative stress in cancer cells as a target for cancer treatment. *Cancer Treat. Rev.* **35**, 32–46 (2009).
7. Chen, X. *et al.* Copper homeostasis and copper-induced cell death in the pathogenesis of cardiovascular disease and therapeutic strategies. *Cell death dis.* **14:105**, 1–12 (2023).
8. Shanbhag, V. C. *et al.* Copper metabolism as a unique vulnerability in cancer. *Biochim. Biophys. Acta.* **1868**, 118893 (2021).

9. Lelièvre, P., Sancey, L., Coll, J. L., Deniaud, A. & Busser, B. The multifaceted roles of copper in cancer: A trace metal element with dysregulated metabolism, but also a target or a bullet for therapy. *Cancers* **12**, 1–25 (2020).
10. Kim, B. E., Nevitt, T. & Thiele, D. J. Mechanisms for copper acquisition, distribution, and regulation. *Nat. Chem. Biol.* **4**, 176–185 (2008).
11. Chen, W. J. *et al.* Regulatory roles of six-transmembrane epithelial antigen of the prostate family members in the occurrence and development of malignant tumors. *Front. Cell Dev. Biol.* **9**, 752426 (2021).
12. Eisses, J. F. & Kaplan, J. H. The mechanism of copper uptake mediated by human CTR1. *J. Biol. Chem.* **280**, 37159–37168 (2005).
13. Turski, M. L. & Thiele, D. J. New roles for copper metabolism in cell proliferation, signaling, and disease. *J. Biol. Chem.* **284**, 717–721 (2009).
14. Chen, G. F. *et al.* Copper transport protein Antioxidant-1 promotes inflammatory neovascularization via chaperone and transcription factor function. *Sci. Rep.* **5**, 14780 (2015).
15. Banci, L. *et al.* Affinity gradients drive copper to cellular destinations. *Nature* **465**, 645–648 (2010).
16. Lasorsa, A. *et al.* Mechanistic and structural basis for inhibition of copper trafficking by platinum anticancer drugs. *J. Am. Chem. Soc.* **141**, 12109–12120 (2019).
17. Dodani, S. C., Leary, S. C., Cobine, P. A., Winge, D. R. & Chang, C. J. A targetable fluorescent sensor reveals that copper-deficient *SCO1* and *SCO2* patient cells prioritize mitochondrial copper homeostasis. *J. Am. Chem. Soc.* **133**, 8606–8616 (2011).
18. Hatori, Y., Inouye, S. & Akagi, R. Thiol-based copper handling by the copper chaperone Atox1. *IUBMB Life* **69(4)**, 246–254 (2017).
19. Gupte, A. & Mumper, R. J. Elevated copper and oxidative stress in cancer cells as a target for cancer treatment. *Cancer Treat. Rev.* **35**, 32–46 (2009).
20. Yang, G. M. *et al.* Structures of the human Wilson disease copper transporter ATP7B. *Cell Rep.* **42**, 112417 (2023).
21. Harris, E. D., Reddy, M. C. M., Majumdar, S. & Cantera, M. Pretranslational control of Menkes disease gene expression. *BioMetals* **16**, 55–61 (2003).
22. Baldari, S., Rocco, G. Di & Toietta, G. Current biomedical use of copper chelation therapy. *Int. J. of Mol. Sci.* **21**, 1069, (2020).
23. Gupta, S. K., Shukla, V. K., Vaidya, M. P., Roy, S. K. & Gupta, S. Serum and tissue trace elements in colorectal cancer. *J. Surg. Oncol.* **52**, 172–175 (1993).
24. Zhang, X. & Yang, Q. Association between serum copper levels and lung cancer risk: A meta-analysis. *Int. J. Med. Res.* **46**, 4863–4873 (2018).

25. Dabek, J. T., Harkonen, M., Adlercreutz, H. & Hyvönen-Dabek, M. Evidence for increased non-ceruloplasmin copper in early-stage human breast cancer serum. *Nutr. Cancer* **17**, 195–201 (1992).
26. Turecký, L., Kalina, P., Uhlíková, E., Námerová, Š. & Křižko, J. Serum Ceruloplasmin and copper levels in patients with primary brain tumors. *Klin. Wochenschr.* **62**, 187-189 (1984).
27. Fang, A. P. *et al.* Serum copper and zinc levels at diagnosis and hepatocellular carcinoma survival in the Guangdong Liver Cancer Cohort. *Int. J. Cancer* **144**, 2823–2832 (2019).
28. Ge, E. J. *et al.* Connecting copper and cancer: from transition metal signalling to metalloplasia. *Nat. Rev. Cancer*, **22**, 102–113 (2022).
29. Feng, Z. *et al.* Artificial intracellular filaments. *Cell Rep. Phys. Sci.* **1**, 100085 (2020).
30. Davies, K. M., Mercer, J. F. B., Chen, N. & Double, K. L. Copper dyshomeostasis in Parkinson's disease: Implications for pathogenesis and indications for novel therapeutics. *Clin. Sci.* **130**, 565–574 (2016).
31. Cui, L. *et al.* Mitochondrial copper depletion suppresses triple-negative breast cancer in mice. *Nat. Biotechnol.* **39**, 357–367 (2021).
32. Roth, P. *et al.* Supramolecular assembly guided by photolytic redox cycling. *Nat. Synth* **2**, 980–988 (2023).
33. Rigo, A., Corazza, A., Paolo, M. L., Rossetto, M., Ugolini, R. & Scarpa, M. Interaction of copper with cysteine: stability of cuprous complexes and catalytic role of cupric ions in anaerobic thiol oxidation. *J. Inorg. Biochem.* **98**, 1495-1501 (2004).
34. Hider, R. C., Kupryszewski, G., Rekowski, P. & Lammek, B. Origin of the positive 225-230 nm circular dichroism band in proteins. Its application to conformational analysis. *Biophys. Chem.* **31**, 45-51 (1988).
35. Joshi, V., Shivach, T., Yadav, N. & Rathore, A. S. Circular dichroism spectroscopy as a tool for monitoring aggregation in monoclonal antibody therapeutics. *Anal. Chem.* **86**, 11606–11613 (2014).
36. Xiao, Z. *et al.* Unification of the copper(I) binding affinities of the metallo-chaperones Atx1, Atox1, and related proteins: Detection probes and affinity standards. *J. Biol. Chem.* **286**, 11047–11055 (2011).
37. Bros, J., Fontaine, S. L., Wedd, A. G. & Xiao, Z. Redox sulfur chemistry of the copper chaperon Atox1 is regulated by the enzyme glutaredoxin 1, the redox potential of the glutathione couple GSSG/2GSH and the availability of Cu(I). *Metallomics* **6**, 793-808 (2014).
38. Karginova, O. *et al.* Inhibition of copper transport induces apoptosis in triple-negative breast cancer cells and suppresses tumor angiogenesis. *Mol. Cancer Ther.* **18** (5), 873–885 (2019).
39. Ramchandani, D. *et al.* Copper depletion modulates mitochondrial oxidative phosphorylation to impair triple negative breast cancer metastasis. *Nat. Commun.* **12**, 7311 (2021).

40. Gao, Y., Shi, J., Yuan, D. & Xu, B. Imaging enzyme-triggered self-assembly of small molecules inside live cells. *Nat. Commun.* **3**, 1033 (2012).
41. Jeena, M. T. *et al.* Mitochondria localization induced self-assembly of peptide amphiphiles for cellular dysfunction. *Nat. Commun.* **8**, 26 (2017).
42. Blockhuys, S. & Wittung-Stafshede, P. Roles of copper-binding proteins in breast cancer. *Int. J. of Mol. Sci.* **18**, 871 (2017).
43. Liu, Yi., Wang, J. & Jiang, M. Copper-related genes predict prognosis and characteristics of breast cancer. *Front. Immunol.* **14**, 1145080 (2023).
44. Wong, P. C. *et al.* Copper chaperone for superoxide dismutase is essential to activate mammalian Cu/Zn superoxide dismutase. *PNAS* **97**, 2886-2891 (2000).
45. Tainer, J. A., Getzoff, E. D., Richardson, J. S. & Richardson, D. C. Structure and mechanism of copper, zinc superoxide dismutase. *Nature* **306**, 284-287 (1983).